PCCP

Check for updates

Unveiling the atomistic mechanisms for oxygen intercalation in a strongly interacting graphene–metal interface†

Carlos Romero-Muñiz, [ID] ‡[a] Ana Martín-Recio,‡[b] Pablo Pou,[ac] José M. Gómez-Rodríguez [ID] *[bcd] and Rubén Pérez [ID] *[ac]

The atomistic mechanisms involved in the oxygen (O) intercalation in the strongly interacting graphene (G) on Rh(111) system are characterized in a comprehensive experimental and theoretical study, combining scanning tunneling microscopy and density functional theory (DFT) calculations. Experimental evidence points out that the G areas located just above the metallic steps of the substrate are the active sites for initializing the intercalation process when some micro-etching points appear after molecular oxygen gas exposure. These regions are responsible for both the dissociation of the oxygen molecules and the subsequent penetration to the G–metal interface. Unlike in other species, the DFT calculations exclude single-point defects as additional entry paths to the interface. After penetration, the intercalation proceeds inwards due to the high mobility of atomic oxygen at the interface following mid-height paths connecting the higher areas of the rippled graphene structure. At larger coverages, the accumulation of O atoms under the high areas increases the G–metal distance in the neighboring low areas, paving the way for the O incorporation and the G detachment that leads to the final O-(2 × 1) structure. Furthermore, our results show that these mechanisms are possible only at temperatures slightly lower than those in which graphene etching takes place.

1 Introduction

The outstanding properties of graphene[1–4] have promoted this one atom thick layer, since its isolation by Novoselov *et al.*,[5] as one of the most promising materials for future technological applications. Large and high quality G flakes[6,7] can be produced, in an easy and economical way, by chemical vapor deposition (CVD) growth on transition metal surfaces. This epitaxial G/metal configuration[6–11] has obvious advantages for device applications and spectroscopic studies. However, the same reactivity of the metal surfaces that promotes growth may represent a fundamental limitation because of the changes induced in the G structure and electronic properties.[12,13] While in the weakly interacting cases

(such as Au(111),[14] Cu(111)[6] and Pt(111)[8,15]), the G layer remains flat and the Dirac cones are preserved – only rigidly shifted towards positive or negative energies –, for strongly interacting metals (such as Ru(0001),[10] Rh(111)[9,16] or Re(0001)[17]), the metal substrate induces a large (∼1 Å) corrugation on the graphene layer and breaks the characteristic linear dispersion of the Dirac cones through a stronger hybridization of the π-G band with the metal d states.

Intercalation of different atoms or molecules in the G–substrate interface is an easy and versatile way to tune the G binding and recover its electronic[18–22] properties. Successful intercalations of many different elements on several graphene supported systems have been reported, including O on Ru(0001),[23–25] Ir(111),[26–29] Pt(111),[29] SiC(0001),[19] Ni(111)[30,31] or Rh(111),[32] Au on SiC(0001),[33] Ge on SiC(0001),[34] H on SiC(0001),[35,36] Al on Ni(111),[37,38] and Cs and Eu on Ir(111).[20,39–41] The basic, simple picture explaining the feasibility of the intercalation process is based on the chemically inert character of graphene: the extra species prefer to react with the surface underneath instead of adsorbing on or damaging the graphene sheet.

This apparently simple chemical process requires, in reality, a combination of different possible steps that are individually challenging, which may include: (i) adsorption and diffusion of the intercalants; (ii) molecular dissociation – when these

[a] Departamento de Física Teórica de la Materia Condensada, Universidad Autónoma de Madrid, E-28049 Madrid, Spain. E-mail: ruben.perez@uam.es
[b] Departamento de Física de la Materia Condensada, Universidad Autónoma de Madrid, E-28049 Madrid, Spain. E-mail: josem.gomez@uam.es
[c] Condensed Matter Physics Center (IFIMAC), Universidad Autónoma de Madrid, E-28049 Madrid, Spain
[d] Instituto Nicolás Cabrera, Universidad Autónoma de Madrid, E-28049 Madrid, Spain

elements are introduced in their molecular form –; (iii) penetration towards the G–substrate interface, and (iv) diffusion inside the interface until they cover the whole G–substrate area. Furthermore, all these individual steps have to be accomplished below the graphene etching temperature, which in our case was ∼570 K. These steps have been studied in detail in the intercalation of oxygen in the weakly interacting G/Ir(111) system by R. Larciprete et al.[26] and T. Michely's group.[27,28,42] In this case, and for oxygen pressures around 10^{-6} Torr, the presence of an incomplete graphene layer on top of the Ir(111) surface facilitates two of the necessary steps to achieve a successful intercalation: oxygen dissociates on the bare metal and, then, starts diffusing towards the G/Ir interface through the graphene edges at $T \sim 500$ K. Beyond this specific system, very little is known about the detailed atomistic mechanisms supporting the different steps of the oxygen intercalation process. Although these mechanisms have been explored for other intercalants, like Si in G/Ru(0001),[43,44] they may substantially differ due to the higher reactivity of the oxygen species.

Here, we contribute to fill this gap with a comprehensive microscopic characterization of the intercalation of oxygen on the strongly interacting G/Rh(111) system,[9,32,45] where the metal substrate is initially fully covered by G. Our previous study[32] combined scanning tunneling microscopy (STM), low energy electron diffraction (LEED) and density functional theory (DFT) calculations to show that the intercalation was feasible and how the process could be followed through the evolution of the STM apparent corrugation. Now, we use the same combination of techniques to unveil the atomic-scale mechanisms that lie behind the different steps involved in the intercalation process. Our results show that (1) O_2 dissociation takes place on those G areas just above the metallic steps, where some micro-etching points appear during oxygen exposure; (2) the subsequent penetration proceeds through these etching points where small bare metal regions emerge; (3) oxygen is highly mobile at the interface, following specific paths that avoid the lower moiré areas; and (4) at larger coverages, the accumulation of O atoms in the high areas increases the G–metal distance in the neighboring areas, paving the way for the incorporation of the O into those lowest areas and the G detachment that leads to the completion of the O-(2 × 1) structure, the final stage of intercalation. All these processes have energy barriers below 1.4 eV and thus can be thermally activated at the intercalation temperature ($T \sim 550$ K), considering a typical attempt frequency of 10^{13} Hz. The understanding of these mechanisms at the atomic scale will shed new light on relevant fields like graphene oxidation and corrosion, coating and membrane technology or heterogeneous catalysis, all of them with potential industrial applicability.

2 Methods

Experiments

All the experiments and measurements were carried out in an ultra-high vacuum (UHV) system with a base pressure below 1×10^{-10} Torr. Our Rh(111) single crystal was prepared by cycles of Ar$^+$ sputtering at 1 keV and annealing at 1200 K while keeping the sample under an oxygen atmosphere to avoid carbide formation at the surface from carbon segregation from the bulk (2×10^{-7} Torr). The sample was then completely covered with a well grown graphene layer by low pressure (2×10^{-7} Torr) chemical vapor deposition (CVD) of ethylene (C_2H_4) at 1100 K. Several rotational domains with different sizes are observed in the STM experiments leading to different moiré patterns with the Rh(111) substrate.[9] These moiré patterns depend then on the relative orientation of the carbon atoms with respect to the metallic ones. Among all of them, the 0° orientation predominates and its moiré is formed by 12 × 12 carbon atoms aligned with 11 × 11 Rh atoms.[9,46] The graphene layer covers the whole metallic surface, leaving no bare metal areas. Also, no large defective areas have been found. The main defects on the sample are the grain boundaries between rotational domains and the step edges in which the graphene shows a higher defect density.

Oxygen intercalation was carried out by exposing the sample to 6×10^{-7} Torr of high purity oxygen gas. In order to activate this process, the sample was kept at ∼550 K, as discussed in the results section of this paper. The characterization of all the intercalation processes and steps was performed in situ by LEED experiments with a four grid analyzer and with a home-built variable temperature STM.[47,48] All STM data were measured and processed with the WSxM software (www.wsxm.es).[49]

First-principles calculations

We have studied in detail the different steps in the oxygen intercalation with an extensive set of DFT calculations on the $[(\sqrt{43} \times \sqrt{43}) - R7.6°]_G$ G/Rh(111) moiré unit cell.[9] This moiré reproduces the main features of the large $[(12 \times 12) - R0°]_G$ moiré commonly found in the experiments and, thanks to its smaller size, makes the DFT study feasible. The analysis of the oxygen diffusion at the interface has been complemented with energy barrier calculations on the $[(\sqrt{91} \times \sqrt{91}) - R27°]_G$ moiré, that includes some small areas with intermediate G–metal separations joining the high parts as in the $(12 \times 12)_G$ moiré, and simulations for atomic O adsorption on those medium-height regions in the $(12 \times 12)_G$ moiré.

We used the VASP code[50] with the plane wave basis set corresponding to a 400 eV energy cutoff, projected augmented wave pseudopotentials.[51,52] The Perdew–Burke–Ernzerhof approach[53] is used for the electronic exchange–correlation functional supplemented with the DFT-D2 Grimme[54] correction to deal with the dispersion (van der Waals) interactions. The reaction paths as well as the optimal geometries of the transition states were calculated with the Climbing Image Nudged Elastic Band (CI-NEB) method.[55] Further computational details can be found in the ESI.†

3 Results and discussion

3.1 Temperature dependence during oxygen intercalation

The experimental results here shown have been performed, under UHV conditions, on a high quality graphene layer grown

This journal is © the Owner Societies 2018

Phys. Chem. Chem. Phys., 2018, 20, 13370–13378 | 13371
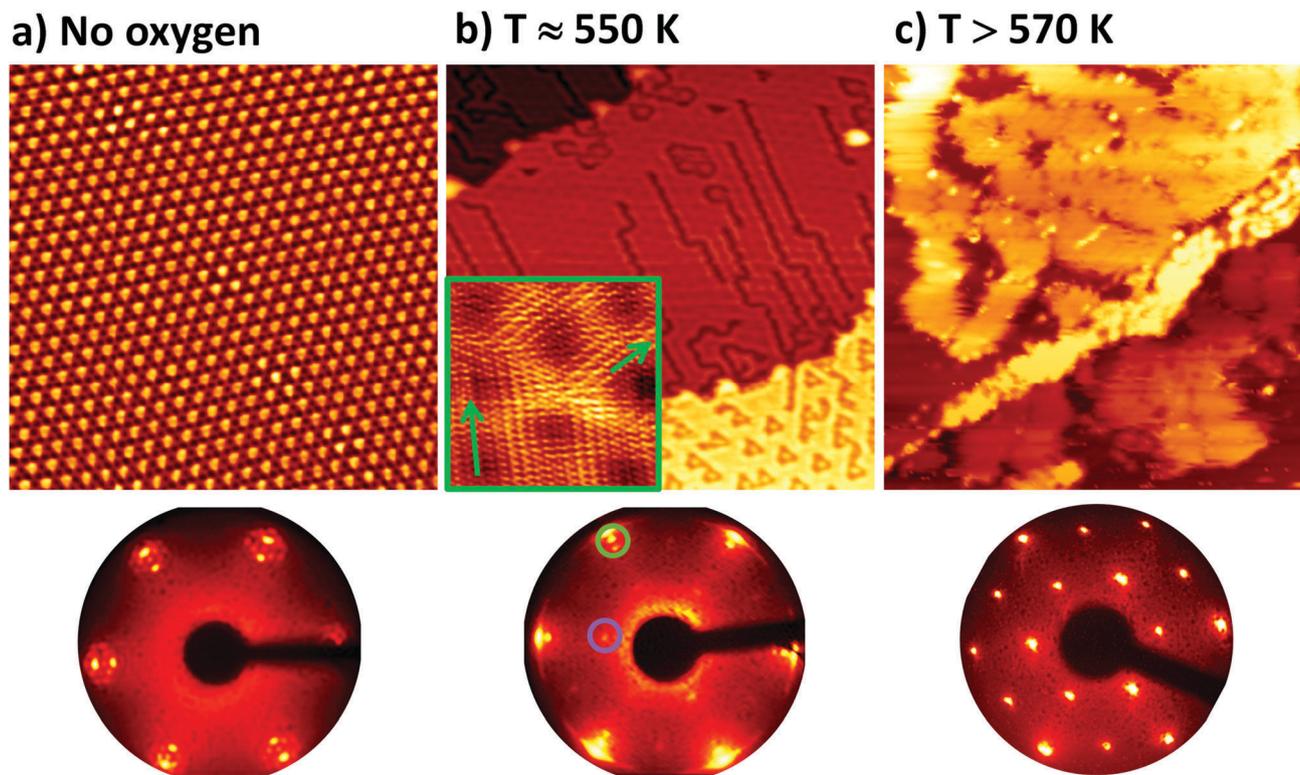
Fig. 1 Temperature dependence of the intercalation process observed through three 60×60 nm^2 STM images and their corresponding LEED experiments. The LEED patterns show: (a) G/Rh(111) moiré spots, (b) the diffuse moiré pattern (green circle) and $2 \times 2/2 \times 1$ (purple circle) spots from the oxygen periodicity, (c) no graphene periodicity but only oxygen $2 \times 2/2 \times 1$ periodicity. The inset in b shows two domains of the 2×1 oxygen structure underneath the graphene. The direction of the compact oxygen rows are indicated by green arrows. (a) -100 mV, 2.5 nA, LEED pattern at 63 eV; (b) 100 mV, 8.6 nA, LEED pattern at 62 eV, inset: 7×7 nm^2, 900 mV, 4.8 nA; (c) 2600 mV, 0.15 nA, LEED pattern at 61 eV.

by CVD that completely covers the Rh(111) single-crystal. Among all the rotational domains of the graphene layer,[9] the $0°$ orientation predominates (Fig. 1a).[9,46]

We have carried out a detailed study on the temperature dependence of the intercalation process. As previously described by other authors for G/Rh(111) and G/Ir(111),[27,56] there is a temperature threshold to activate the oxygen intercalation. This value depends on several factors, including the graphene quality, the CVD molecular precursors and the size of the graphene domains.[27,56] Besides, it is also known that when the temperature is increased beyond a certain value, the graphene oxidation process is enhanced.[56,57] Fig. 1 shows the STM and LEED measurements that have been carried out to determine the optimal temperature range for intercalation. Before introducing oxygen in our chamber, both the LEED and STM results mostly show the preferential moiré pattern formed by the graphene and the Rh(111) surface (Fig. 1a). Then, when the sample is exposed to oxygen gas (6×10^{-7} Torr) and while it is kept at a temperature around 550 K, intercalation takes place. As shown in our previous work,[32] the amount of intercalated oxygen is easily controlled by changing the exposure time (from 30 minutes to observe the very first intercalation stages, to 100 minutes for a completely intercalated oxygen layer). Our LEED measurements provide evidence of the intercalation: they exhibit a new pattern that can only be assigned to a 2×2 structure and/or the

superposition of three rotational domains with 2×1 periodicity. These are the most stable configurations for the O/Rh(111) system. STM images taken by tunneling through G (see the inset in Fig. 1b) prove, in fact, the formation of the three 2×1 rotational domains underneath G (see ESI†). If T is increased above 570 K, the G layer is removed by oxidation and only oxygen remains on the surface as is appreciated on the LEED pattern of Fig. 1c.

The experiments described above show that the temperature window for oxygen intercalation on G/Rh(111) is very narrow. G oxidation takes place very fast at temperatures just slightly larger than the one which enables oxygen intercalation, $T \sim 550$ K. This imposes a stringent limit on the maximum activation energies for all of the microscopic processes involved in the different steps of the intercalation. Following transition state theory, and assuming an attempt frequency of 10^{13} Hz, the energy barriers have to be smaller than ~ 1.4 eV for those processes to be thermally activated.

3.2 Starting intercalation near metallic steps

In order to start the intercalation process, O$_2$ molecules have to dissociate leading to atomic species. In the G/O/Ir(111) system,[27,28,42] the initial presence of bare metal areas facilitates this stage of the intercalation process as molecular oxygen and other small molecules easily dissociate on transition metal surfaces.

This is not the case on free-standing graphene, where the energy barrier for O_2 dissociation is of the order of 3 eV.[58] However, we did observe how intercalation takes place when we expose our fully-covered G/Rh(111) sample to a low partial pressure of oxygen. According to our experimental findings (shown in Fig. 2), intercalation starts in G areas in the neighborhood of the metallic steps located underneath. Although these areas are initially fully covered by the graphene carpet, after the exposure to oxygen gas, STM reveals the appearance of small etched areas where the metal substrate underneath is exposed. The high temperatures – near the etching limit –, the reactivity of the metal atoms at the step, and the strain induced in the G layer that further softens some of the C–C bonds promote the oxidation reaction of these localized G regions, giving rise to the etched area shown in Fig. 2a and highlighted in the inset (see also Fig. S5, ESI†). Therefore, these areas serve as active sites to achieve molecular dissociation following one of these two hypotheses: (1) it takes place on top of the graphene layer, where the possible presence of point-like and extended defects can enhance the chemical reactivity of these areas.[59,60] Or (2), more probably, directly on the bare metal areas of the micro-etching points, where the O_2 dissociation barrier on Rh(111) is ~ 0.2 eV per molecule.[61]

The next step in the intercalation process involves the penetration paths for atomic oxygen towards the G/Rh interface. Studies in similar G/metal systems point out that penetration of intercalants may occur following two different mechanisms: (1) incorporation via graphene edges has been observed in the O intercalation on G/Ir(111)[27] and in the Pb intercalation in G/Ru(0001);[62] while, even in the absence of preexisting graphene

edges or extended defects, (2) penetration can take place through vacancies or other point defects, as reported in experiments on the G/Si/Ru(0001) system.[22,43,44] In the case of G/Rh(111), our DFT calculations show that the penetration of single atoms through point defects like monovacancies or Stone–Wales (SW) defects is very improbable in this strongly interacting system. Although these accession paths would be feasible for oxygen atoms dissociated near graphene defects, the calculated penetration barriers (≥ 3 eV) are too high to be overcome at the experimental temperature window (see more details in Section S3 of the ESI†). We have not considered the possible collective effects involving several oxygen atoms, previously studied in the G/Si/Ru(0001) system,[43] because they also yield large penetration barriers (~ 3 eV). These theoretical results are in agreement with our experimental observations (Fig. 2b) in which the first stages of the intercalation are not observed near grain boundaries (black solid line) in spite of the presence of multiple point-defects.

Since point defects have been excluded as accession points, the oxygen dissociation and the penetration through the interface should happen following some kind of edge-related phenomena involving the very small areas close to the step which have suffered G etching (see the inset of Fig. 2a, displaying O atoms adsorbed on the bare Rh(111)). We have previously shown that, in the first stages of the process, the corrugation of the intercalated areas increases with respect to the non-intercalated ones.[32] Therefore, we can use the STM corrugation to follow the evolution of the intercalation. We have systematically observed that the very first intercalated areas always appear near metal surface defects like the step edges, as shown in Fig. 2a. The density of intercalated atoms clearly reduces as we move away
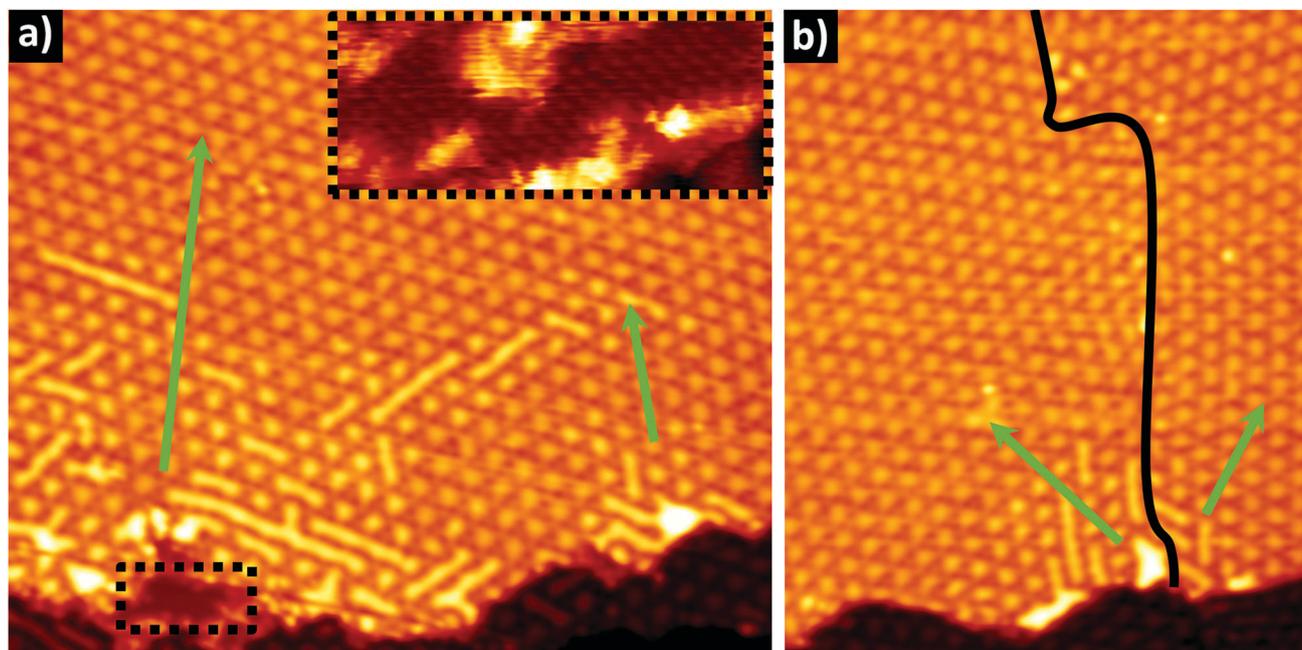
Fig. 2 Intercalation starting process always occurs near metal steps. The first stages of the intercalation are observed in both images and it gradually disappears when we move away from the step edge (green arrows). Also, small areas of graphene etching are observed close to the step edges (inset), helping the intercalation process. (a) 70 × 60 nm² (120 mV, 6.5 nA); inset: 9 × 3.5 nm² (100 mV, 8.6 nA); (b) 52 × 64 nm² (120 mV, 6.5 nA).

from metal step edges (green arrows in Fig. 2) pointing towards the step edges as the entry points. These experimental results indicate that, once these extended defects are created, oxygen can penetrate through the G–metal edges, following the mechanism recently proposed, on the basis of first principles calculations,[63] for metal-passivated G edges on Cu(111) and Ni(111) surfaces. The energy barriers reported[63] for the cleavage of the G–metal bond and the attachment of the first O atom ($\sim$1 eV) and the subsequent O incorporation ($\leq$0.63 eV) are much smaller than the ones we have calculated for penetration through point defects, giving support to our identification of the micro-etching areas as the entry paths for O intercalation.

3.3 Oxygen binding and mobility at the G–metal interface

The next step in the intercalation, after the penetration into the interface, is the diffusion of oxygen atoms between the metal and the G layer. We have to take into account the corrugation of the G layer, that modulates the G–metal surface separation in the moiré unit cell between $\sim$2 Å and $\sim$3 Å. Firstly, we consider the energetics of the adsorption of a single oxygen atom on the metal surface under the graphene. From previous studies,[61,64] we know that the most favorable positions for oxygen atoms in the bare Rh(111) surface correspond to hollow sites, the fcc-hollow positions being slightly more stable than the hcp-hollow sites. As mentioned before, the moiré pattern used in our simulations corresponds to a $\left[(\sqrt{43} \times \sqrt{43}) - R7.6°\right]_{G}$ unit cell, (6×6 with respect to the Rh(111)). There is a total of 36 fcc-hollow and 36 hcp-hollow possible sites, which now are not equivalent due to the presence of the G layer. The upper panel of Fig. 3 shows the relative binding energies of 22 of those hollow sites distributed all over the unit cell. Some of them correspond to hcp-hollow sites that are less favorable than the adjacent fcc-hollow positions (see Table S1 in the ESI†) confirming that the presence of graphene does not alter the tendency found in the bare Rh(111).[64] Moreover, our results reveal how the spatial modulation of the G layer governs the energetic picture. In the high areas of the moiré pattern, with larger G–metal distances, the adsorption is significantly more favorable than that in the low regions, with energy differences up to $\sim$2 eV. No significant variations in the binding energy are observed among different metal-equivalent sites sharing the same G–metal relative distance.

Next, we focus our attention on the mobility of oxygen atoms under the G layer. The diffusion of small adsorbates on clean metallic surfaces takes place by means of jumps between adjacent metal hollow positions, with the transition state corresponding to the bridge adsorption sites. On clean Rh(111), we have obtained diffusion barriers of 0.50 eV and 0.51 eV for oxygen coverages of 1/4 and 1/36 respectively, in agreement with previous calculations,[61] whereas the activation energy for a similar diffusion in free-standing graphene is slightly larger: 0.73 eV.[65] Our calculations confirm that when the oxygen atoms are placed between G and the metallic surface, diffusion processes are still possible at room temperature (RT). Fig. 3 (lower panel) displays the diffusion path of a single oxygen atom along one side of the unit cell, covering both the
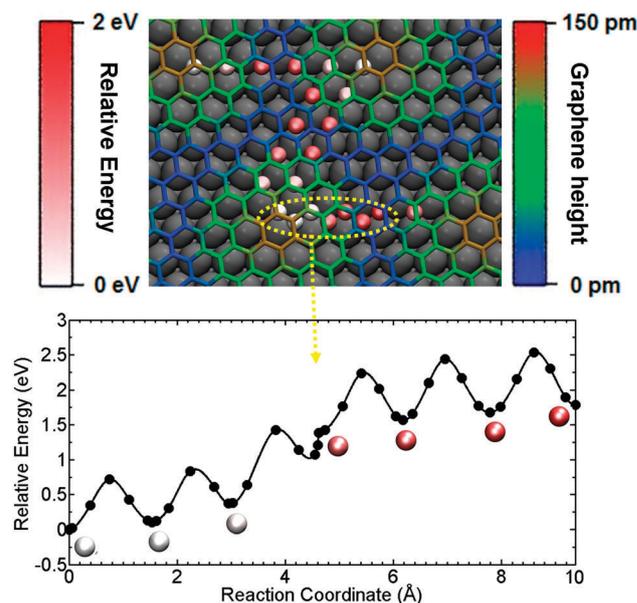
Fig. 3 Adsorption energies and diffusion barriers for O atoms incorporated in the G/Rh(111) interface (calculated on the $\left[(\sqrt{43} \times \sqrt{43}) - R7.6°\right]_{G}$ unit cell). Upper panel: O adsorption energy on the Rh(111) hollow sites and corrugation of the carbon atoms in G/Rh(111) before O incorporation. The blue-green-red color scale displays the relative height of the carbon atoms in the original G/Rh(111) interface, while the white-red color scale of the spheres represents the relative energy of the oxygen atom on that particular site (taking the most stable O adsorption configuration as reference). Lower panel: Diffusion barriers for a single oxygen atom following the path highlighted in yellow in the top panel. Each diffusion step consists of a jump between two adjacent hollow sites.

high and low parts of the moiré pattern. The diffusion barriers under G in the highest moiré areas (0.72 eV) are slightly larger than on the bare Rh(111) surface. However, although the activation barriers for each hollow-hollow jump are always smaller than 1 eV, the modulation in the adsorption energies along the moiré pattern (resulting in a total energy barrier of 2.5 eV) prevents an isolated oxygen atom from intercalating in the lower parts of the moiré.

Therefore, for the small moiré pattern considered so far, a single oxygen atom would not be able to travel through the G/Rh(111) interface because this would always require passing through the lowest part of the moiré (see Fig. 3). However, this is not the case in larger moiré patterns, in particular, in those most commonly found in experiments $(12 \times 12)_{G}$, where there are small areas with intermediate G–metal separations joining the high parts (see Fig. 4). We have explored this in the $\left[(\sqrt{91} \times \sqrt{91}) - R27°\right]_{G}$ moiré, which already shows this feature of the larger moirés. Fig. 4 (left panel) shows the diffusion path for a single jump on a mid-height region whose value is again $\sim$0.7 eV (see Section S5 of ESI† for more details about this calculation). Therefore, the total energy barrier that a single oxygen atom should overcome to go from a high moiré area to the equivalent region of another neighbouring cell results from the combination of these simple jumps plus the adsorption energy difference between the high, E_0 and the mid-height moiré areas, E_1, that is 0.69 eV. This final total barrier (1.4 eV) is low enough for the
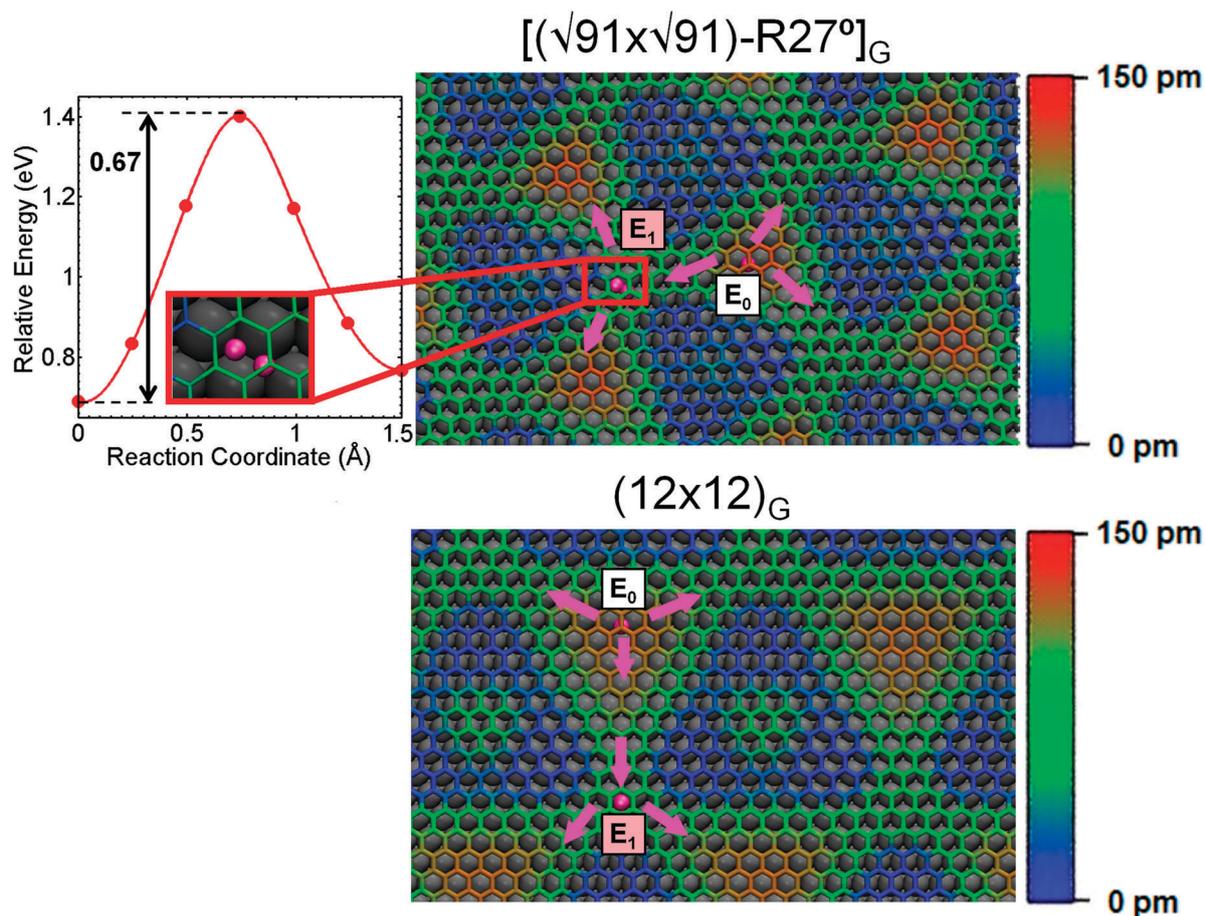
Fig. 4 Mobility of intercalated oxygen atoms in the low coverage regime on the moiré patterns $\left[\left(\sqrt{91} \times \sqrt{91}\right) - R27°\right]_G$ (upper panel) and $(12 \times 12)_G$ (lower panel). The schematic top views (same color code as Fig. 3) show that high areas (with the largest adsorption energy E_0) are linked by less energetically favorable mid-height regions (E_1, green) in these moiré patterns. O atoms can diffuse to neighboring high areas through the mid-height regions (purple arrows) avoiding the most unfavorable low areas of the moire (blue), as the energy barriers for O to jump between two hollow sites are lower than ~ 0.7 eV. This is illustrated with the CI-NEB calculation for the path connecting an fcc and an hcp site in the mid-height region of the $\left[\left(\sqrt{91} \times \sqrt{91}\right) - R27°\right]_G$ moiré. In the inset, the geometries of the initial and final states of the diffusion are depicted. Notice that we have chosen as energy reference the most energetically favorable adsorption site (E_0) instead of E_1. We expect these barriers to be even lower in the $(12 \times 12)_G$ moiré.

process to be thermally activated at the intercalation temperature. This process would be even more favorable on the largest $(12 \times 12)_G$ moiré, where the energy penalty for an oxygen atom to be adsorbed in the mid-height region is smaller, 0.58 eV vs. 0.69 eV, than in the $\left[\left(\sqrt{91} \times \sqrt{91}\right) - R27°\right]_G$ moiré (see Section S5, ESI† for details). These results demonstrate that, in the low coverage limit, oxygen atoms can freely move along different unit cells by traveling from different high areas through mid-height regions. Fig. 4 illustrates this process: an oxygen atom placed on a favorable site could move, following one of the different possible diffusion paths indicated by the arrows, avoiding the lowest parts of the moiré (blue areas) which are clearly energetically unfavorable.

3.4 Collective diffusion and intercalation in the bridge moiré areas

In order to complete the intercalation and the detachment of the G layer from the metal surface, oxygen atoms should penetrate into the lowest moiré regions and diffuse across the

whole interface. We cannot provide a full account of this process with the small moiré that we are considering but we can use it to illustrate the key mechanism. In our previous work,[32] we discussed how the intercalation of one O atom in the highest top moiré areas increases the G–metal separation around it allowing the diffusion and adsorption of new oxygen atoms in this area. This results in the full occupation of the high areas and a larger G corrugation that leads to an increase in the G–metal separation in the neighboring low areas (see Fig. 5). This larger separation paves the way for the intercalation of oxygen and the G detachment on those areas.[32] This process can be actually seen in the STM images (Fig. 2 and S5, ESI†): far from the penetration points, the O atoms are mostly intercalated in the high top moiré areas, but, close to them, stripes are also observed. The presence of O atoms in different high areas proves that, in the first intercalation steps, O atoms are able to migrate between two isolated moiré top areas to another following the mechanism described above. When the O concentration on these areas increases, two adjacent intercalated moiré top
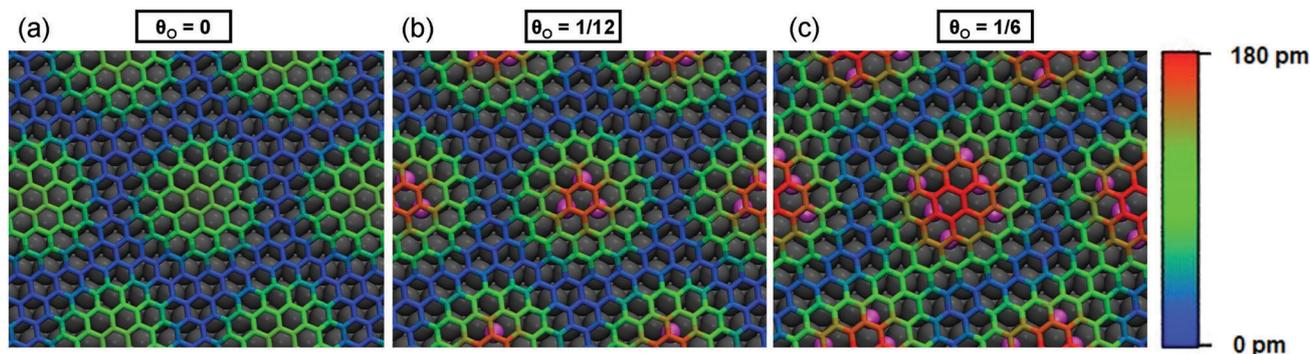
Fig. 5 Height map (in pm) for the carbon atoms belonging to the graphene monolayer for three different oxygen coverages, illustrating the changes induced in the graphene–metal distances in the low areas of the moiré pattern by the increase of the occupation of the high areas. Intercalated oxygen atoms are represented by magenta spheres.

positions are easily linked by the decoupling of the low moiré bridge zones, forming the stripes.

STM images also reveal the collective diffusion of oxygen atoms across different moiré cells at RT. Fig. 6a and b correspond to the same surface region imaged at different times. The collective atomic movement can be clearly observed (green ovals in the zooms shown in Fig. 6c and d). The stripe that forms a T-shaped structure (Fig. 6c) has changed its shape (Fig. 6d) *via* one

of these collective movements of O atoms: the high area below is no longer linked but, in exchange, the stripe has elongated towards the left, connecting to a neighboring high area. These processes of collective diffusion, – that might be enhanced by the interaction with the STM tip during measurements – become more frequent for larger coverages, and lead to the full coverage of the interface with a O-(2 × 1) structure (see ESI†) the step that completes the intercalation.
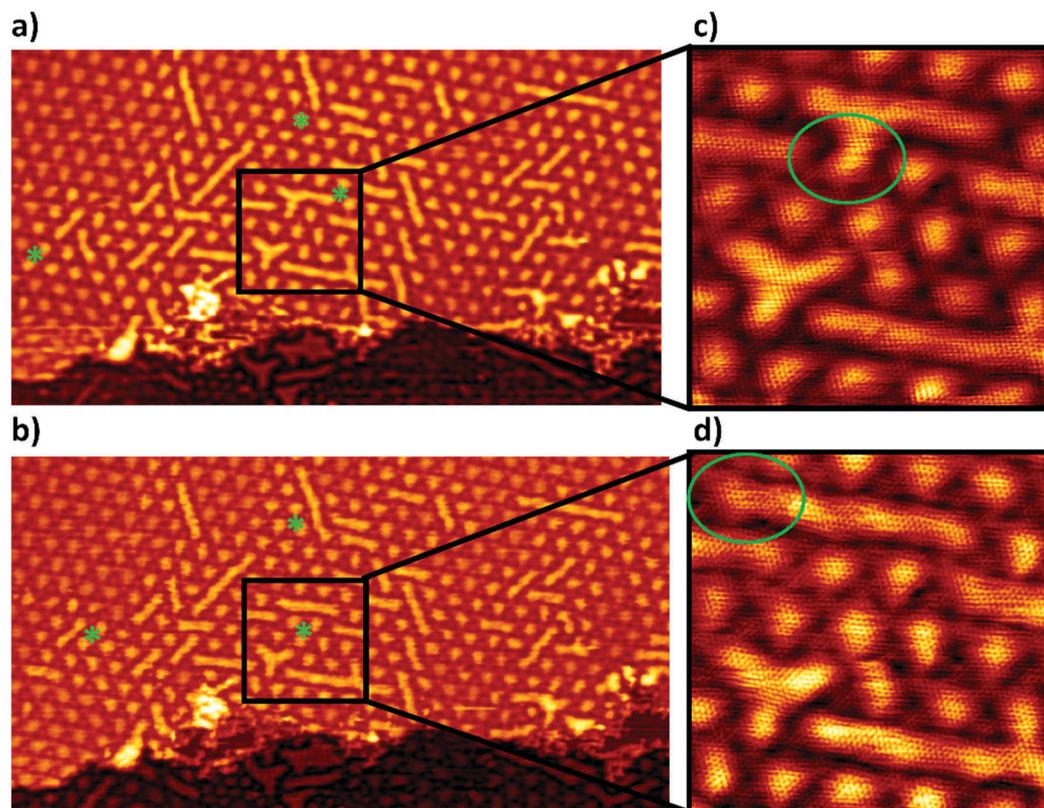
Fig. 6 Experimental observation of the oxygen mobility underneath graphene at room temperature. Both main images (a and b) and zoom-in images (c and d) are from the same area and were taken consecutively. The marked areas (green stars and ovals) show small stripes that change their length or direction from one image to the next one. (a) (80 × 44) nm^2, 0.2 V, 7.1 nA; (b) (80 × 44) nm^2, 0.1 V, 6.5 nA; (c) (14 × 14) nm^2, 0.1 V, 5.9 nA; (d) (14 × 14) nm^2, 0.1 V, 8.6 nA.

4 Conclusions

We have completed a comprehensive study of the atomistic processes involved in the oxygen intercalation on the strongly interacting graphene/Rh(111) through STM experiments, LEED measurements and DFT calculations. All these processes have energy barriers below 1.4 eV and thus can be thermally activated at the intercalation temperature ($T \sim 550$ K). Our work shows that the graphene areas near the metallic steps are responsible for the activation of the whole intercalation process. Despite starting from a fully-covered graphene sample, local G etching takes place, close to the metallic steps underneath, after oxygen exposure, exposing small bare metal areas. These areas act both as the active sites for the dissociation of molecular oxygen, and, subsequently, as accession paths to the G/Rh interface. Therefore, bare metal areas, that seem to be essential in weakly interacting cases, are no longer needed in the highly coupled G/Rh system. Our DFT calculations discard point defects such as monovacancies or Stone–Wales defects as possible additional penetration paths to the interface. Once at the interface, the oxygen atoms are highly mobile, following intermediate height moiré patches that connect the high areas. At larger coverages, the accumulation of O atoms in the high areas increases the G–metal distance in the neighboring areas, paving the way for the incorporation of the O into those lower areas and the G detachment that leads to the final O-(2×1) structure.

Conflicts of interest

The authors declare no competing financial interest.

Acknowledgements

References

1 K. S. Novoselov, A. K. Geim, S. V. Morozov, D. Jiang, M. I. Katsnelson, I. V. Grigorieva, S. V. Dubonos and A. A. Firsov, *Nature*, 2005, **438**, 197.

2 A. K. Geim and K. S. Novoselov, *Nat. Mater.*, 2013, **6**, 183.

3 C. Lee, X. Wei, J. W. Kysar and J. Hone, *Science*, 2008, **321**, 385.

4 A. H. Castro Neto, F. Guinea, N. M. R. Peres, K. S. Novoselov and A. K. Geim, *Rev. Mod. Phys.*, 2009, **81**, 109–162.

5 K. S. Novoselov, A. K. Geim, S. V. Morozov, D. Jiang, Y. Zhang, S. V. Dubonos, I. V. Grigorieva and A. A. Firsov, *Science*, 2004, **306**, 666–669.

6 A. J. Martínez-Galera, I. Brihuega and J. M. Gómez-Rodríguez, *Nano Lett.*, 2011, **11**, 3576.

7 A. T. N'Diaye, J. Coraux, T. N. Plasa, C. Busse and T. Michely, *New J. Phys.*, 2008, **10**, 043033.

8 M. M. Ugeda, D. Fernández-Torre, I. Brihuega, P. Pou, A. J. Martínez-Galera, R. Pérez and J. M. Gómez-Rodríguez, *Phys. Rev. Lett.*, 2011, **107**, 116803.

9 A. Martín-Recio, C. Romero-Muñiz, A. J. Martinez-Galera, P. Pou, R. Pérez and J. M. Gómez-Rodríguez, *Nanoscale*, 2015, **7**, 11300–11309.

10 P. W. Sutter, J. I. Flege and E. A. Sutter, *Nat. Mater.*, 2008, **7**, 406.

11 Y. S. Dedkov, M. Fonin, U. Rüdiger and C. Laubschat, *Phys. Rev. Lett.*, 2008, **100**, 107602.

12 M. Batzill, *Surf. Sci. Rep.*, 2012, **67**, 83.

13 H. Tetlow, J. P. de Boer, I. Ford, D. Vvedensky, J. Coraux and L. Kantorovich, *Phys. Rep.*, 2014, **542**, 195–295.

14 S. Nie, N. C. Bartelt, J. M. Wofford, O. D. Dubon, K. F. McCarty and K. Thürmer, *Phys. Rev. B: Condens. Matter Mater. Phys.*, 2012, **85**, 205406.

15 P. Merino, M. Švec, A. L. Pinardi, G. Otero and J. A. Martín-Gago, *ACS Nano*, 2011, **5**, 5627.

16 B. Wang, M. Caffio, C. Bromley, H. Früchtl and R. Schaub, *ACS Nano*, 2010, **4**, 5773.

17 E. Miniussi, M. Pozzo, A. Baraldi, E. Vesselli, R. R. Zhan, G. Comelli, T. O. Menteş, M. A. Niño, A. Locatelli, S. Lizzit and D. Alfè, *Phys. Rev. Lett.*, 2011, **106**, 216101.

18 J. A. Robinson, M. Hollander, M. LaBella, K. A. Trumbull, R. Cavalero and D. W. Snyder, *Nano Lett.*, 2011, **11**, 3875–3880.

19 S. Oida, F. R. McFeely, J. B. Hannon, R. M. Tromp, M. Copel, Z. Chen, Y. Sun, D. B. Farmer and J. Yurkas, *Phys. Rev. B: Condens. Matter Mater. Phys.*, 2010, **82**, 041411.

20 M. Petrović, I. Šrut Rakić, S. Runte, C. Busse, J. T. Sadowski, P. Lazić, I. Pletikosić, Z.-H. Pan, M. Milun, P. Pervan, R. Atodiresei, N. Brako, D. Šokčević, T. Valla, T. Michely and M. Kralj, *Nat. Commun.*, 2013, **4**, 2772.

21 C. Enderlein, Y. S. Kim, A. Bostwick, E. Rotenberg and K. Horn, *New J. Phys.*, 2010, **12**, 033014.

22 Q. Fu and X. Bao, *Chem. Soc. Rev.*, 2017, **46**, 1842.

23 P. Sutter, J. T. Sadowski and E. A. Sutter, *J. Am. Chem. Soc.*, 2010, **132**, 8175–8179.

24 A. Dong, Q. Fu, M. Wei, Y. Liu, Y. Ning, F. Yang, H. Bluhm and X. Bao, *Surf. Sci.*, 2015, **634**, 37–43.

25 E. Voloshina, N. Berdunov and Y. Dedkov, *Sci. Rep.*, 2008, **6**, 20285.

26 R. Larciprete, S. Ulstrup, P. Lacovig, M. Dalmiglio, M. Bianchi, F. Mazzola, L. Hornekær, F. Orlando, A. Baraldi, P. Hofmann and S. Lizzit, *ACS Nano*, 2012, **6**, 9551–9558.

27 E. Grånäs, J. Knudsen, U. A. Schröder, T. Gerber, C. Busse, M. A. Arman, K. Schulte, J. N. Andersen and T. Michely, *ACS Nano*, 2012, **6**, 9951–9963.

28 A. J. Maríez-Galera, U. A. Schroder, F. Huttmann, W. Jolie, F. Craes, C. Busse, V. Caciuc, N. Atodiresei, S. Blugel and T. Michely, *Nanoscale*, 2016, **8**, 1932.

29 I. Palacio, G. Otero-Irurueta, C. Alonso, J. I. Martínez, E. López-Elvira, I. M. noz Ochando, H. J. Salavagione, M. F. López,

This journal is © the Owner Societies 2018

Phys. Chem. Chem. Phys., 2018, **20**, 13370–13378 | **13377**

M. García-Hernández, J. Méndez, G. J. Ellis and J. A. Martín-Gago, *Carbon*, 2018, **129**, 837.

30 Y. Dedkov, W. Klesse, A. Becker, F. Späth, C. Papp and E. Voloshina, *Carbon*, 2017, **121**, 10.

31 L. Bignardi, P. Lacovig, M. M. Dalmiglio, F. Orlando, A. Ghafari, L. Petaccia, A. Baraldi, R. Larciprete and S. Lizzit, *2D Mater.*, 2017, **4**, 025106.

32 C. Romero-Muñiz, A. Martín-Recio, P. Pou, J. M. Gómez-Rodríguez and R. Pérez, *Carbon*, 2016, **101**, 129.

33 I. Gierz, T. Suzuki, R. T. Weitz, D. S. Lee, B. Krauss, C. Riedl, U. Starke, H. Höchst, J. H. Smet, C. R. Ast and K. Kern, *Phys. Rev. B: Condens. Matter Mater. Phys.*, 2010, **81**, 235408.

34 K. V. Emtsev, A. A. Zakharov, C. Coletti, S. Forti and U. Starke, *Phys. Rev. B: Condens. Matter Mater. Phys.*, 2011, **84**, 125423.

35 C. Riedl, C. Coletti, T. Iwasaki, A. A. Zakharov and U. Starke, *Phys. Rev. Lett.*, 2009, **103**, 246804.

36 F. Speck, J. Jobst, F. Fromm, M. Ostler, D. Waldmann, M. Hundhausen, H. B. Weber and T. Seyller, *Appl. Phys. Lett.*, 2011, **99**, 122106.

37 A. A. Rybkina, A. G. Rybkin, A. V. Fedorov, D. Y. Usachov, M. E. Yachmenev, D. E. Marchenko, O. Y. Vilkov, A. V. Nelyubov, V. K. Adamchuk and A. M. Shikin, *Surf. Sci.*, 2013, **609**, 7.

38 E. N. Voloshina, A. Generalov, M. Weser, S. Böttcher, K. Horn and Y. S. Dedkov, *New J. Phys.*, 2011, **13**, 113028.

39 S. Schumacher, T. O. Wehling, P. Lazić, S. Runte, D. F. Förster, C. Busse, M. Petrović, M. Kralj, S. Blügel, N. Atodiresei, V. Caciuc and T. Michely, *Nano Lett.*, 2013, **13**, 5013–5019.

40 S. Schumacher, D. F. Förster, M. Rösner, T. O. Wehling and T. Michely, *Phys. Rev. Lett.*, 2013, **110**, 086111.

41 S. Schumacher, F. Huttmann, M. Petrović, C. Witt, D. F. Förster, C. Vo-Van, J. Coraux, A. J. Martínez-Galera, V. Sessi, I. Vergara, R. Rückamp, M. Grüninger, N. Schleheck, F. Meyer zu Heringdorf, P. Ohresser, M. Kralj, T. O. Wehling and T. Michely, *Phys. Rev. B: Condens. Matter Mater. Phys.*, 2014, **90**, 235437.

42 U. A. Schröder, E. Grånäs, T. Gerber, M. A. Arman, A. J. Martínez-Galera, K. Schulte, J. N. Andersen, J. Knudsen and T. Michely, *Carbon*, 2016, **96**, 320–331.

43 Y. Cui, J. Gao, L. Jin, J. Zhao, D. Tan, Q. Fu and X. Bao, *Nano Res.*, 2012, **5**, 352–360.

44 G. Li, H. Zhou, L. Pan, Y. Zhang, L. Huang, W. Xu, S. Du, M. Ouyang, A. C. Ferrari and H.-J. Gao, *J. Am. Chem. Soc.*, 2015, **137**, 7099–7103.

45 A. B. Preobrajenski, M. L. Ng, A. S. Vinogradov and N. Mårtensson, *Phys. Rev. B: Condens. Matter Mater. Phys.*, 2008, **78**, 073401.

46 E. N. Voloshina, Y. S. Dedkov, S. Torbrügge, A. Thissen and M. Fonin, *Appl. Phys. Lett.*, 2012, **100**, 241606.

47 O. Custance, S. Brochard, I. Brihuega, E. Artacho, J. M. Soler, A. M. Baró and J. M. Gómez-Rodríguez, *Phys. Rev. B: Condens. Matter Mater. Phys.*, 2003, **67**, 235410.

48 A. J. Martínez-Galera and J. M. Gómez-Rodríguez, *J. Phys. Chem. C*, 2011, **115**, 11089.

49 I. Horcas, R. Fernández, J. M. Gómez-Rodríguez, J. Colchero, J. Gómez-Herrero and A. M. Baró, *Rev. Sci. Instrum.*, 2007, **78**, 013705.

50 G. Kresse and J. Furthmüller, *Phys. Rev. B: Condens. Matter Mater. Phys.*, 1996, **54**, 11169–11186.

51 G. Kresse and D. Joubert, *Phys. Rev. B: Condens. Matter Mater. Phys.*, 1999, **59**, 1758–1775.

52 P. E. Blöchl, *Phys. Rev. B: Condens. Matter Mater. Phys.*, 1994, **50**, 17953–17979.

53 J. P. Perdew, K. Burke and M. Ernzerhof, *Phys. Rev. Lett.*, 1996, **77**, 3865–3868.

54 S. Grimme, *J. Comput. Chem.*, 2006, **27**, 1787–1799.

55 G. Henkelman, B. P. Uberuaga and H. Jónsson, *J. Chem. Phys.*, 2000, **113**, 9901.

56 K. Gotterbarm, W. Zhao, O. Hofert, C. Gleichweit, C. Papp and H.-P. Steinrück, *Phys. Chem. Chem. Phys.*, 2013, **15**, 19625–19631.

57 E. Starodub, N. C. Bartelt and K. F. McCarty, *J. Phys. Chem. C*, 2010, **114**, 5134–5140.

58 S. Ni, Z. Li and J. Yang, *Nanoscale*, 2012, **4**, 1184.

59 D. W. Boukhvalov and M. I. Katsnelson, *Nano Lett.*, 2008, **8**, 4373.

60 F. Banhart, J. Kotakoski and A. V. Krasheninnikov, *ACS Nano*, 2011, **5**, 26.

61 O. R. Inderwildi, D. Lebiedz, O. Deutschmann and J. Warnatz, *J. Chem. Phys.*, 2005, **122**, 034710.

62 L. Jin, Q. Fu, R. Mu, D. Tan and X. Bao, *Phys. Chem. Chem. Phys.*, 2011, **13**, 16655–16660.

63 L. Ma, X. C. Zeng and J. Wang, *J. Phys. Chem. Lett.*, 2015, **6**, 4099.

64 M. V. Ganduglia-Pirovano and M. Scheffler, *Phys. Rev. B: Condens. Matter Mater. Phys.*, 1999, **59**, 15533–15543.

65 A. M. Suarez, L. R. Radovic, E. Bar-Ziv and J. O. Sofo, *Phys. Rev. Lett.*, 2011, **106**, 146802.